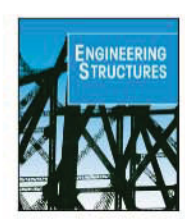


Contents lists available at ScienceDirect

Engineering Structures

journal homepage: www.elsevier.com/locate/engstruct



Deflection reduction of the guideway of aerial PRT systems by horizontal supports

Linda Teka, Liming Li, Huiming Yin*

Columbia University, Department of Civil Engineering and Engineering Mechanics, 610 Seeley W. Mudd 500 West 120th Street, New York, 10027, NY, USA

ARTICLE INFO

Keywords: Beam theory Axial tensile loading Green's function Nonlinear deflection Boundary conditions Personal rapid transit (PRT)

ABSTRACT

Controlling the deflection of the aerial personal rapid transit (PRT) structure is crucial to the system's riding comfort and energy efficiency. A nonlinear elastic analysis of a beam under combined axial and transverse loads is conducted to show a new mechanism to stiffen the PRT structure by using horizontal support. Although the classic beam theory often neglects the effect of the tensile axial force, when the deflection caused by the transverse load is large, the tensile axial force may significantly contribute to the mitigation of overall deflection, particularly for thin, long beams. Using the governing equation of beam with an axial force, the Green's function is obtained for different boundary conditions. To demonstrate and validate the theory, three-point bending tests have been conducted for three boundary conditions: (1) two roller supports with a varying horizontal load; (2) two clamped supports with a varying horizontal load; and (3) two fixed supports with rigid constraints, which passively induce a tensile force by the transverse load. The formulation captures the nonlinear elastic behavior of the beams with horizontal constraints or axial forces, which shows that the maximum deflection of the 11 beams can reduce 38%–87% under the elastic load range. The Green's function can be applied to arbitrary transverse loads in structural design. A smart cushion system is invented to provide horizontal support to the guideway of a lightweight, stiffened aerial PRT structure.

1. Introduction

Transportation networks are multifaceted structures that enable the continuous flow of people and goods. Due to the growing population and the number of private vehicles, there has been an increase in traffic congestion, delays, gas prices, and vehicular gas emissions, causing major concern in many cities around the world [1,2]. To improve the current transportation system, researchers have suggested various transportation systems that mainly focus on mass transit, of which the Personal Rapid Transit (PRT) was first proposed by Donn Fichter [3]. Aerial PRT is a public transport mode featuring small automated vehicles operating on a network of specially built guideway systems [4,5], which can be integrated into existing transportation infrastructure systems with solar roof for energy harvesting and roadway protection [2]. Passengers can board the automated vehicle upon arriving at a station and, with a sufficiently extensive network of tracks, take relatively direct routes to their destination without stops [6,7].

The research community has primarily focused on the modeling and control of PRT [8–11]. However, the structural design and integrity of PRT infrastructure have not been well studied. In aerial PRT structures, due to the relatively long load-transfer path from the rail, to beam, to girder, to column, and then to foundation, the sagging of the rail under

the loading of the automated vehicles will be particularly important for riding comfort, energy efficiency, and safety. The rail beams are usually designed for the deflection serviceability requirement using the classic Bernoulli–Euler (B–E)'s beam theory, which does not consider the significant effect of axial restraints on the deflection of beams when the gap between rail beams is well controlled. Thereby, the deflection may be overly estimated with an inefficient design and material wastage.

Several beam theories have been developed by different researchers in the past [12–15], and the simplest and most widely used one is the B–E beam theory [16]. Timoshenko's theory of beams improves the B–E theory by including the effect of the shear stresses on the deformation and relaxes the normality assumption of plane sections that keep normal to the deformed center line or neutral plane [17–19]. The Timoshenko beam theory requires the shear correction factors to compensate for the error due to this constant shear stress assumption. The shear correction factors depend not only on the material and geometric parameters but also on the loading and boundary conditions [19].

Both beam theories give analytical solutions for the deflection of a beam subjected to only transverse loading [12,16] and the effects of the axial force have often been disregarded. However, Timoshenko and Woinowsky-Krieger incorporated the effect of axial load in the analysis

E-mail address: yin@civil.columbia.edu (H. Yin).

^{*} Corresponding author.

of plates [12]. In many applications, when the support points provide horizontal constraints, axial tensile force induced by the support will produce nonlinear effects on the elastic behavior of the beam when the curvature becomes considerable, which stiffens the beam and lowers the deflection. This nonlinear elastic behavior can lead to an optimized design and lightweight structures.

Nonlinear deflection has been observed for simply supported large building integrated photovoltaic modules in solar roof applications, as horizontal constraints are required for leakage prevention [20,21]. In addition, The case of offshore pipes and static pressure pipes that are hooked by anchors [22,23] can be modeled as beams subjected to combined transverse and tensile axial loading. High-fidelity design and analysis require simultaneously considering the effect of both loads: axial tension tends to straighten the beam, thus counteracting the bending moments produced by the transverse load. It is significant for the research community and industry practitioners to derive the nonlinear elastic solution of a beam subjected to both transversal and axial loading, which corresponds to multiple real-world conditions where beams are subjected to both bending and stretching.

Few researchers have studied the deflection of beams subjected to both transversal and axial loads. Kristoffersen et al. [23,24] investigated the bending of pressurized and un-pressurized steel pipes due to a transverse load while simultaneously applying three axial tensile loads. The paper considered three types of axial loads: no axial load, a constant axial load, and a linearly increasing axial load. They conducted experiments and numerical simulations and concluded that a tensile axial force increases a pipe's resistance to transverse bending. A series of experimental tests on hollow rectangular stainless-steel beams under combined loading was conducted by Zhao et al. [25,26]. Cicirello and Palmeri [27] performed a static analysis of beams with multiple unilateral cracks under combined axial and transverse loads; the study led to analytical solutions with constants that can be determined using the boundary conditions.

The ultimate resistance and failure patterns can be greatly altered by the membrane force effects introduced by constraints [28]. Researchers [28–30] have studied the stiffening effect of horizontal constraints on beams and slabs. The analytical solution for estimating the capacity of fully clamped slabs was suggested by Chen et al. [30]. The solution incorporated the membrane action and studied the effect of membrane action on the load-carrying capacity of the clamped slab. The study showed that the load-deflection relationships of fully clamped reinforced concrete slabs could be accurately represented by considering compressive–tensile membrane effects.

In addition, the experimental work on hybrid fiber reinforced-lightweight aggregate concrete beams [28], investigated the effect of membrane forces on the beam's capacities, by introducing member forces through specifically designed clamps. The experimental results showed that the ultimate load of the beams could be substantially underestimated if membrane forces were neglected. Chen et al. [29] introduced a simplified membrane action theory by modifying the maximum membrane force design method to predict the total static resistance-deflection curves of restrained beam–slab reinforced concrete structures. The paper also conducted experimental tests on constrained beams, and the results showed that the static load-carrying capacity and membrane force increased with the enhancement of the restraint stiffness.

This paper investigated the nonlinear effect of tensile axial load on the deflection of beams. Considering the straightening effect of axial tensile loads on beams, the Green's function caused by a unit point force is formulated for different boundary conditions. The deflection for an arbitrarily distributed load can be derived by the integral of the Green's function. Specifically, analytical solutions for three different boundary conditions were determined: (1) roller-supported beams on two roller supports with varying tensile axial load, (2) end-clamped beams clamped at both ends with varying axial load, and (3) fixed-end

supported beams with rigid constraints at both ends, which induce a tensile force in the horizontal plane by the transverse load.

The analytical solutions were further validated by the experimental results in which a transversal point load is applied at the mid-span of the beams with three boundary conditions. In Case 3, when the restrained beams were subjected to a transversal point load, horizontal forces were created due to the change in length. These horizontal forces reduced the curvature of the beam and led to a nonlinear deflection. The existing beam design [13,16] do not consider the effect of horizontal forces on the deflection of beams, thereby overestimating the deflection of fully restrained beams. The present formulation can be used in the design and analysis of beams, and the formulation can be extended to different boundary conditions.

The remainder of this paper first states the problem in Section 2. Section 3 reviews the beam theory and formulates the governing equation of beam bending under both transverse and horizontal loads. The Green's functions for the three kinds of boundary conditions are derived, and can be used for arbitrarily distributed transverse loads. Section 4 introduces the experimental design and setups for three testing configurations. Section 5 shows the comparisons between the experimental results and the theoretical prediction, which demonstrates that the present formulation can predict the experimental results very well while the B–E theory cannot capture the nonlinear deflection. Section 6 shows the applications of the present formulation in the design of a lightweight rail for the aerial PRT system [2,31], in which a smart mounting system is invented to provide the horizontal support for nearly seamless guideways.

2. Problem statement

PRT is an energy-efficient electric transit system that combines the beneficial characteristics of personal automobiles, the advantages of public transportation, and clean technologies for a sustainable transit system [7,32]. Fig. 1 shows the design of a solar aerial PRT system, which exhibits the following features [2,31]:

- Additional transit mode of lightweight vehicles alleviates congestion by taking advantage of aerial space.
- Computer-aided sensing and control systems guarantee nonstop routes to the destination for riders through infrastructurevehicle-rider communications.
- Solar energy harvested from its building integrated photovoltaic (BIPV) roof can power lightweight vehicles and charge surface electric vehicles.
- The roof structure provides shade for roadway and surface traffic protection from ultraviolet (UV) and temperature degradation as well as rain or snow influence.

While PRT has significant advantages in regard to efficiency and sustainability, there are also challenges that need to be addressed. The design of PRTs is also very complex, having to incorporate the characteristics of the PRT system with the traffic demand, accessibility, city aesthetic, and space availability. In addition, regular maintenance of the infrastructure is essential as it affects the ride quality. The vehicles travel along a network of guideways, which are rail beams supported by columns, and the deflection of these beams impacts comfort causes safety concerns, and affects the visual aesthetic. Therefore, for economic, architectural, and community benefits, it is desirable to design a lightweight and seamless guideway system with a larger span, in which the deflection under the traffic load can be a controlling factor for energy efficiency, riding comfort, and structural safety.

The BIPV roof structure can be designed according to the existing building codes for wind, snow, earthquake, and service loads [33,34]. However, the load transfer from a vehicle to the guideway beam, girder, and column, and finally, the foundation shall be carefully investigated and designed. As the vehicle size will be well controlled by using lightweight materials mainly for thermal and acoustic insulation,

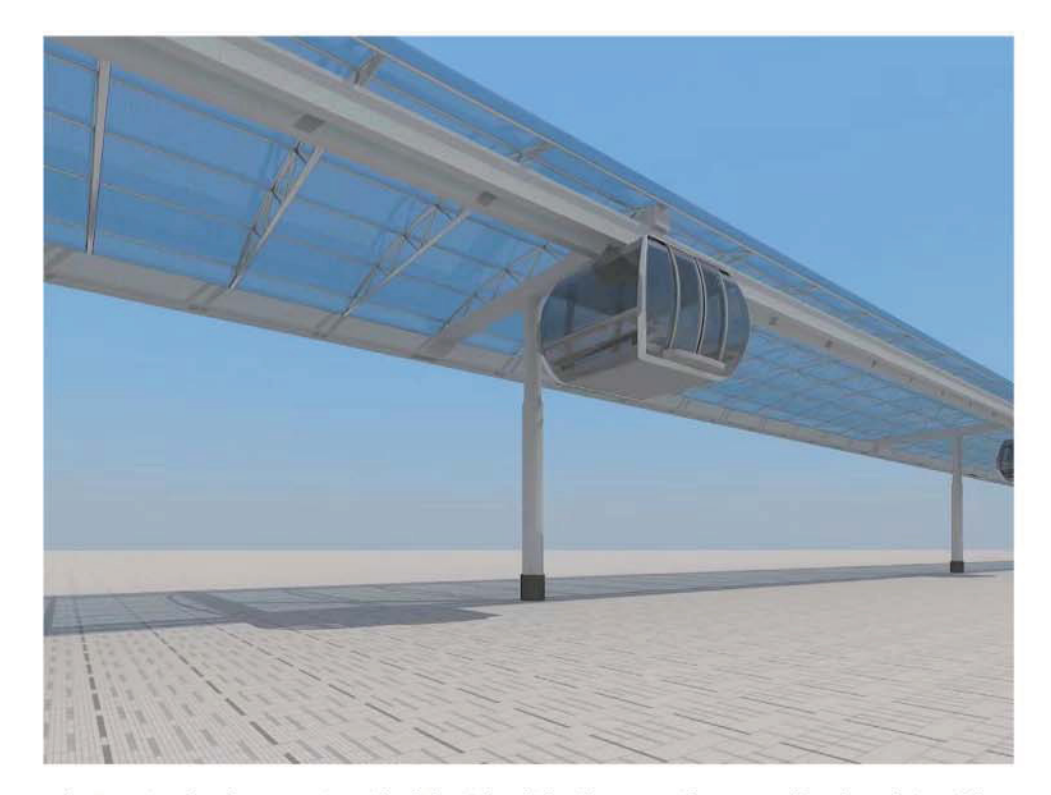


Fig. 1. Design of a solar PRT section with a lightweight vehicle riding on a guideway covered by photovoltaic modules.

a 4–6 rider vehicle will be in a range of 900–1200 kg, including riders, which shall be considered in the living loads for the stress analysis in the structural design. However, to minimize the weight of the guideway with a large span of 10–50 m, the deflection of rail beams shall be specially considered.

In this paper, we focus on the deflection of these rail beams due to vehicular loads. While the vehicular loads are dynamic in reality, we considered the critical condition that the vehicular load is located at the middle span for the worst-case scenario with the maximum deflection. A simplified one-span beam is used in this paper to represent the PRT rail beams, and a concentrated point load is applied at the mid-span to represent the vehicular load.

Consider the geometry of the beam with cross-sectional area A, a moment of inertia I, length L, and height H; mechanical properties including Young's modulus E, shear modulus G and yield strength σ^y ; the loads on the rail beam including the uniformly distributed load Q and the point load Q at the midpoint of the beam. The deformation of the beam will depend on the boundary conditions. Three types of boundary conditions are considered:

- 1. The beam is rested on the girder by simple supports with horizontal constraints to avoid the railing collapse in shortening;
- The beam is clamped with the neighboring beams for a continuous guideway on the girder with small temperature expansion cushions to avoid a bulging effect;
- The beam is welded with the neighboring beams by a rigid connection on the girder, which is perfectly continuous but requires a large horizontal force to keep the geometry.

The three connection conditions can be idealized as the simple, clamped, and fixed supports, respectively, but each exhibits a horizontal force P to keep the gap between the beams nearly zero for structural stability, noise control, and riding comfort. Each connection condition exhibits advantages and disadvantages in the construction cost, deflection control, maintenance, and load capacity, which will be revisited in Section 6, subsequently.

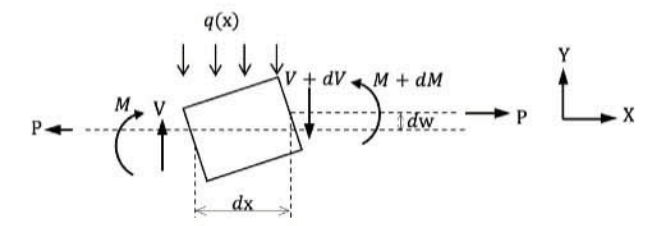


Fig. 2. An infinitesimally small beam segment of length dx.

3. Formulation

3.1. Governing equation and general solution

Consider an infinitesimally small segment of the beam of length dx, as shown in Fig. 2, that is subjected to a distributed transversal load, q(x), and a tension force, P, which is assumed to be applied at the centroid of the cross-section. The deflection, dw, is the displacement in the y-direction of any point on the axis of the beam. To include the effect of the axial force on the deflection of a beam, equilibrium is considered in the displaced configuration.

The equilibrium of forces in the vertical direction gives:

$$V - (V + dV) - q(x)dx = 0$$

$$\tag{1}$$

$$\frac{dV}{dx} = -q(x) \tag{2}$$

Moment equilibrium about the rightmost edge at the neutral axis yields:

$$-M - V dx + M + dM - P dw + q(x) dx \frac{dx}{2} = 0$$
 (3)

The square of the infinitesimally small length of dx is a higher-order term that will be neglected. By rearranging the terms,

$$V = \frac{dM}{dx} + P\frac{dw}{dx} \tag{4}$$

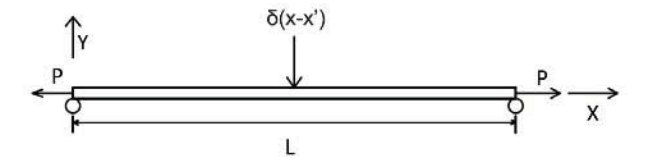


Fig. 3. A roller-supported beam subjected to both axial and transversal load.

According to the moment-curvature relation,

$$M = -EI\frac{d^2w}{dv^2} \tag{5}$$

Substituting Eqs. (2) and (4) into Eq. (5), the governing equation can be written as.

$$EI\frac{d^4w}{dx^4} - P\frac{d^2w}{dx^2} = q(x) \tag{6}$$

In order to simplify the derivation, a dimensionless parameter is defined as $\alpha^2 = \frac{P}{EI}$. And the governing equation can be rewritten as,

$$\frac{d^4w}{dx^4} - \alpha^2 \frac{d^2w}{dx^2} = \frac{q(x)}{EI} \tag{7}$$

which can be found in the literature [12,21,35]. Solving the above ordinary differential equation with boundary conditions, one can obtain the deflection and then stress distribution. There are two types of solution: the trigonometric functions can fit the differential equation in the series form [12], which produces artificial oscillation and requires many terms to approach the accurate solution; whereas the exponential function or hyperbolic function exhibits simplicity and accuracy [21, 35]. This paper uses the second one. For example, when a uniform load $q(x) = q_0$ is applied, the deflection solution can be obtained as:

$$w(x) = C_3 \sinh \alpha x + C_2 \cosh \alpha x + C_1 x + C_0 - \frac{q_0 x^2}{2P}$$
(8)

where C_0 , C_1 , C_2 , and C_3 are constants that can be determined by using the boundary conditions. The first four terms form the general solution, and the last term is the particular solution to the governing equation.

When an arbitrary load is applied to the beam, the deflection can be obtained by the Green's function of the beam [36,37]. Therefore, the constants in Eq. (8) can be directly obtained by the Green's function as follows because the Green's function satisfies the boundary conditions already.

3.2. Green's function for roller supported beams

In this section, a case of the roller-supported beam shown in Fig. 3 that is subjected to a unit concentrated transversal load at an arbitrary point x', namely $q(x) = \delta(x - x')$, and a tensile axial load, P, is considered.

For a simply supported beam, the boundary conditions are given by the deflection and moment at the supporting ends as

$$w(0) = w(L) = 0$$
 (9)

$$w''(0) = w''(L) = 0$$
 (10)

The deflection can be represented by the Green's function G(x, x'), which denotes the deflection at any point x caused by a unit point force at x' as:

$$\frac{d^4G}{dx^4} - \alpha^2 \frac{d^2G}{dx^2} = \frac{\delta(x - x')}{EI} \tag{11}$$

in which the deflection and its first derivative, or slope, shall be continuous. Similarly to Eq. (8), the Green's function can be written in terms of the general solution and particular solution as follows:

$$EIG(x, x') = C_3 \sinh \alpha x + C_2 \cosh \alpha x + C_1 x + C_0$$

$$+ \frac{\sinh \alpha(x-x') - \alpha(x-x')}{\alpha^3} H(x-x') \tag{12}$$

where H(x - x') is the Heaviside function, and C_0 , C_1 , C_2 , and C_3 are constants that will be determined by using the boundary conditions of Eq. (9) and (10), or

$$G(0, x') = G(L, x') = 0;$$
 $G''(0, x') = G''(L, x') = 0$ (13)

By applying Eq. (13) to the Green's function in Eq. (12), the constants C_i , (i = 0, 1, 2, 3) are obtained as follows.

$$C_0 = C_2 = 0;$$
 $C_1 = \frac{1}{\alpha^2} (1 - \frac{x'}{L});$ $C_3 = -\frac{1}{\alpha^3} \frac{\sinh \alpha (L - x')}{\sinh \alpha L}$ (14)

Therefore the Green's function for a roller-supported beam subjected to a transverse point load placed anywhere along the length L is simplified as:

$$EIG(x, x') = -\frac{\sinh \alpha (L - x')}{\alpha^3 \sinh \alpha L} \sinh \alpha x + \frac{1 - \frac{x'}{L}}{\alpha^2} x + \frac{\sinh \alpha (x - x') - \alpha (x - x')}{\alpha^3} H(x - x')$$
(15)

For a roller-supported beam subjected to a point load of Q_0 at the mid-span, namely x'=L/2, the Green's function Eq. (15) can further be simplified to provide the deflection function as $w(x)=Q_0G(x,L/2)$, or:

$$w(x) = \frac{Q_0}{EI} \left[\frac{x}{2\alpha^2} - \frac{\sinh \alpha x}{2\alpha^3 \cosh \frac{\alpha L}{2}} + \frac{\sinh \alpha (x - \frac{L}{2}) - \alpha (x - \frac{L}{2})}{\alpha^3} H(x - \frac{L}{2}) \right]$$
(16)

where the maximum deflection is at the mid-span, x = L/2, as follows:

$$w(L/2) = \frac{Q_0}{2EI} \left(\frac{L}{2\alpha^2} - \frac{\tanh\frac{\alpha L}{2}}{\alpha^3}\right)$$
 (17)

Given an arbitrarily distributed load q(x), the deflection function can be provided by the integral of the Green's function as follows:

$$w(x) = \frac{1}{EI} \int_{-L=0}^{L} G(x, x')q(x')dx'$$
(18)

For example, the simply supported beam under a uniformly distributed load $q(x)=q_0$ can be derived by the above integral as:

$$w(x) = \frac{q_0}{\alpha^4 EI} \left(\frac{\cosh \alpha (\frac{L}{2} - x)}{\cosh \frac{\alpha L}{2}} - 1 \right) + \frac{q_0 x(L - x)}{2\alpha^2 EI}$$
 (19)

Alternatively, using the classic B–E beam theory, the deflection of a simply supported beam subjected to a concentrated transversal load, Q_0 , at the mid-span can be calculated using the green's function as follows:

The B–E beam formula for a unit load applied at x = X' can be written as,

$$EI\frac{d^4w}{dx^4} = EI\frac{d^4G}{dx^4} = \delta(x - x')$$
 (20)

After integration, the Green's function is obtained as

$$G(x,x') = \frac{(x-x')^3}{6}H(x-x') + \frac{c_1x^3}{6} + \frac{c_2x^2}{2} + c_3x + c_4$$
 (21)

By substituting the boundary conditions in Eq. (13), the deflection equation for a roller-supported beam subjected to a point load of Q_0 loaded at x' = L/2 is,

$$w = \frac{Q_0}{EI} \left(\frac{\left(x - \frac{L}{2}\right)^3}{6} H\left(x - \frac{L}{2}\right) - \frac{x^3}{12} + \frac{L^2 x}{16} \right)$$
 (22)

The maximum deflection at L = x/2 is,

$$w(x) = \frac{Q_0 L^3}{48EI} \tag{23}$$

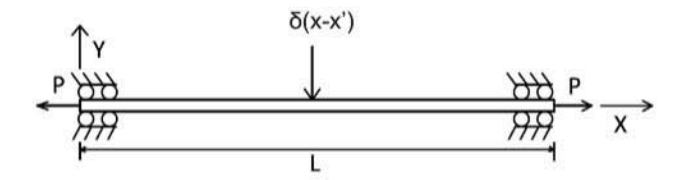


Fig. 4. A double clamped beam subjected to both axial and transversal load.

3.3. Green's function for double clamped beam

Consider a beam with both ends clamped and subjected to a concentrated transversal load and tensile axial loads, as shown in Fig. 4.

Following the same procedure in Section 3.2, the deflection can be represented by the Green's function G(x,x') in Eq. (12), where C_0, C_1, C_2 , and C_3 are to be determined by using the following boundary conditions:

$$G(0, x') = G(L, x') = 0;$$
 $G'(0, x') = G'(L, x') = 0$ (24)

By substituting Eq. (12) into Eq. (24), the constants $C_i(i=0,1,2,3)$ are calculated for G(x,x') as,

$$\begin{split} C_2 &= \frac{[\cosh \alpha (L-x') - 1] (\sinh \alpha L - \alpha L) - [\sinh \alpha (L-x') - \alpha (L-x')] (\cosh \alpha L - 1)}{\alpha^3 [(\cosh \alpha L - 1)^2 - \sinh \alpha L (\sinh \alpha L - \alpha L)]} \\ C_3 &= -\frac{\cosh \alpha (L-x') - 1 + \alpha^3 C_2 \sinh \alpha L}{\alpha^3 (\cosh \alpha L - 1)} \\ C_1 &= -C_3 \alpha \\ C_0 &= -C_2 \end{split}$$

(25)

The constants calculated above can be substituted into Eq. (12) to get the Green's function for double-clamped beams. For a clamped beam with a point load at the mid-span, the constants C_i , i = 0, 1, 2, 3 can be simplified for G(x, 1/2) as;

$$C_0 = -\frac{\cosh\frac{\alpha L}{2} - 1}{2\alpha^3 \sinh\frac{\alpha L}{2}}; \quad C_1 = \frac{1}{2\alpha^2}; \quad C_2 = \frac{\cosh\frac{\alpha L}{2} - 1}{2\alpha^3 \sinh\frac{\alpha L}{2}}; \quad C_3 = -\frac{1}{2\alpha^3}$$
 (26)

which leads to the Green's function for double clamped beam with a point load at the mid-span as follows:

$$EIG(x, 1/2) = -\frac{1}{2\alpha^3} \sinh \alpha x + \frac{\cosh \frac{\alpha L}{2} - 1}{2\alpha^3 \sinh \frac{\alpha L}{2}} \cosh \alpha x + \frac{x}{2\alpha^2}$$

$$-\frac{\cosh \frac{\alpha L}{2} - 1}{2\alpha^3 \sinh \frac{\alpha L}{2}} + \frac{\sinh \alpha (x - x') - \alpha (x - x')}{\alpha^3} H(x - x')$$
(27)

Similarly, for a clamped beam subjected to a point load of Q_0 at the mid-span, namely x'=L/2, the Green's function in Eq. (27) can provide the deflection function as $w(x)=Q_0G(x,L/2)$, or:

$$w(x) = \frac{Q_0}{2EI\alpha^3} \left[\alpha x - \sinh \alpha x + \frac{(\cosh \alpha x - 1)(\cosh \frac{\alpha L}{2} - 1)}{\sinh \frac{\alpha L}{2}} + \frac{\sinh \alpha (x - \frac{L}{2}) - \alpha (x - \frac{L}{2})}{\alpha^3} H(x - \frac{L}{2}) \right]$$
(28)

The maximum deflection, occurring at the mid-span of $x = \frac{L}{2}$, can be simplified into:

$$w(L/2) = \frac{Q_0(l\alpha - 4\tanh\frac{L\alpha}{4})}{4\alpha^3 EI}$$
 (29)

In addition, the deflection function for an arbitrarily distributed load q(x) can be provided by the integral of the Green's function

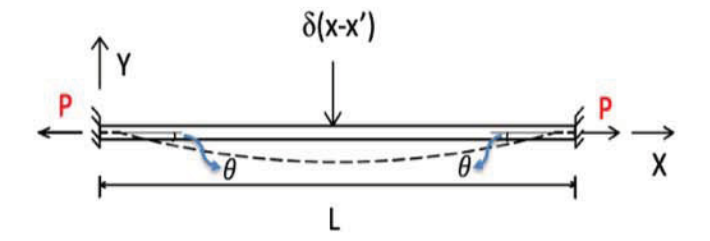


Fig. 5. Deflection of a restrained beam and the membrane force created.

Eq. (18). The deflection for a distributed load $q(x) = q_0$ is obtained as

$$w(x) = \frac{q_0 L}{2\alpha^3 EI} \frac{\cosh\frac{L\alpha}{2} \left(1 - \frac{2x}{L}\right) - \cosh\frac{L\alpha}{2}}{\sinh\frac{L\alpha}{2}} + \frac{q_0 x(L - x)}{2\alpha^2 EI}$$
(30)

3.4. Nonlinear elastic behavior for beams with rigid supports

Consider a beam of length, L, with horizontal, vertical, and rotational constraints at both ends in Fig. 5. It is equivalent to the clamped beam with a certain axial force P to make the horizontal displacement to be zero. When a transverse load, Q_0 , is applied, the beam undergoes a deflection w(x) in the downward direction, causing the beam to curl as shown in Fig. 5. The change of length caused by the curvature of the beam leads to a membrane force P, in the axial direction. Therefore, although no additional horizontal forces are applied, the rigid supports will produce the horizontal force with the increase of the transverse force, which causes a non-linear deformation of the beam.

Similarly, by considering symmetry, the governing equation and boundary conditions for a beam with rigid constraints are similar to the case of double-clamped beams, resulting in a similar deflection equation Eq. (28).

After the application of the axial load, the beam curls up, resulting in a slope, θ , which results in a small length change. The projected horizontal length of the deflected beam is given by,

$$L_{x} = \int_{0}^{L} \cos\theta ds \tag{31}$$

The change of length of a beam due to bending, i.e., the difference between its original length and the horizontal projection of the curved beam, can be determined by the slope function [38];

$$\lambda = L - L_x = \int_0^L (1 - \cos\theta) \approx \int_0^L \frac{1}{2} (\frac{dw}{dx})^2 dx$$
 (32)

Based on displacement compatibility, the axial elongation of the beam is equal to the change of length λ , which is written as,

$$\lambda = \frac{PL}{EA} \tag{33}$$

Equating Eqs. (32) and (33), the characteristic equation for α can be written as

$$\frac{2\alpha^2 LI}{A} = \int_0^L (\frac{dw}{dx})^2 dx \tag{34}$$

Finally, the value of α can be numerically solved using Eqs. (28) and (34); subsequently, the deflection can be calculated using Eq. (28).

The above analysis can be generalized to the simply supported beam with rigid supports, in which Eq. (16) shall be used. However, the experimental studies in this paper focus on fixed supports only.

As a reference of the classic B–E beam theory without horizontal supports (P=0), the deflection of a fixed end beam subjected to a concentrated transversal load, Q_0 at the midpoint is,

$$w(x) = \frac{Q_0 L x^2}{16EI} - \frac{Q_0 x^3}{12EI}$$
(35)

Table 1

Material description of 11 beams of 4 groups tested under three setups: Groups A and B for simply supported, C for clamped, and D for fixed ends.

| Group | Name | Material | Width (mm) | Depth (mm) | Length (mm) | σ_y (MPa) | E (GPa) |
|---------|------|------------------|------------|------------|-------------|------------------|---------|
| Group A | A1 | low carbon steel | 12.7 | 6.35 | 596.9 | 345 | 200 |
| | A2 | low carbon steel | 12.7 | 6.35 | 596.9 | 345 | 200 |
| | A3 | low carbon steel | 12.7 | 6.35 | 596.9 | 345 | 200 |
| Group B | B1 | low carbon steel | 12.7 | 1.5875 | 546.1 | 250 | 200 |
| | B2 | low carbon steel | 12.7 | 1.5875 | 546.1 | 250 | 200 |
| | В3 | low carbon steel | 12.7 | 1.5875 | 546.1 | 250 | 200 |
| Group C | C1 | low carbon steel | 12.7 | 1.5875 | 274.3 | 250 | 200 |
| | C2 | low carbon steel | 12.7 | 1.5875 | 274.3 | 250 | 200 |
| | C3 | low carbon steel | 12.7 | 1.5875 | 274.3 | 250 | 200 |
| Group D | D1 | Aluminum | 25.4 | 3.378 | 226 | 276 | 69 |
| | D2 | Aluminum | 25.4 | 3.225 | 226 | 276 | 69 |

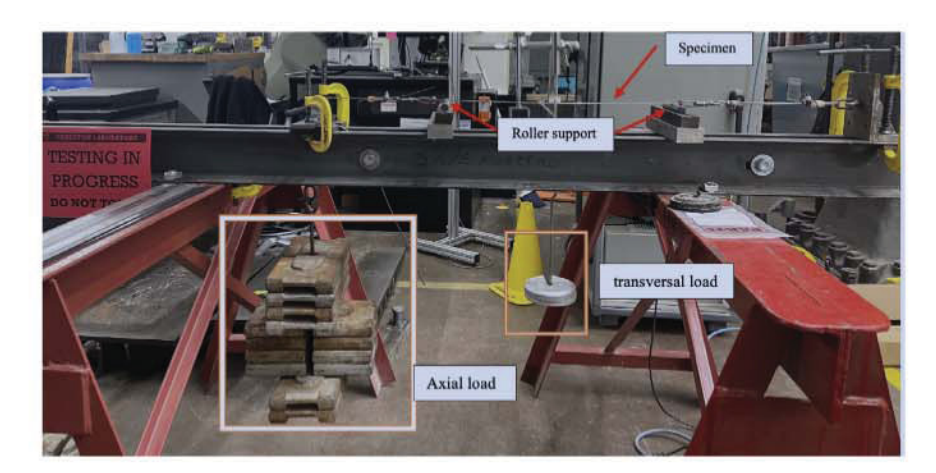


Fig. 6. A simply supported beam specimen mounted on a bending and axial stretching test setup.

which disregards the effect of the axial force P so that the clamped beam and fixed beam share the same form of the deflection function.

In the following sections, analytical solutions will be calculated using the new formulation Eq. (28) and will be compared to the deflection calculated using the B–E solution in Eq. (35). The new formulation accounts for the effect of the induced axial tensile force leading to a non-linear defection, while the latter fails to take into account the straightening effect of the axial load and thereby overestimating the deflection of restrained beams.

4. The experimental design and testing

4.1. Experimental plan and material properties

Three different experimental tests using low-carbon steel and aluminum specimens were conducted at the Carlton Laboratory at Columbia University, with the aim of investigating the effect of axial loads and horizontal restraints on the deflection of beams with various boundary conditions. A total of 11 beams, 6 roller-supported, 3 double-clamped, and, 2 fully restrained beams, were tested. The roller-supported and double-clamped beams were subjected to a concentrated load at mid-span and horizontal tensile axial loads. The fully restrained beam was subjected to a concentrated load at mid-span through the three-point bending testing.

The specimen tested in the experiment are grouped into four groups, Group A, B, C, and D. Group A, B, and C are tested for a combined loading, concentrated load at mid-span and axial tensile loading at both ends, while Group D was tested for three-point loading with the fixed ends. The beams in Groups A and B are roller-supported beams, while Group C consists of double-clamped beams, with rotational and vertical translation restraints at both ends. Group D consists of rigid supports at the fixed end against rotational, vertical, and horizontal translation. The properties of these steel specimens used are summarized in Table 1 below.

4.2. Experimental setups for combined transversal and axial tensile loading

A test setup capable of applying an axial load while at the same time bending a specimen transversely was designed and assembled in the Carlton laboratory at Columbia University. This setup was used to test the roller-supported and double-clamped beams and is shown in Figs. 6 and 7, respectively. The maximum deflection of the beam was recorded by using a transducer that was placed at the mid-span.

A load hanger is placed at the mid-span to load the beam transversely (three-point bending). To apply the axial load, on the left-hand side of the beam, a wire connects the specimen to a load hanger by passing through a pully. While on the right-hand side, the beam is connected to a fixed fixture, thereby subjecting it to a tensile reaction force.

The transversal load was applied first by placing load heads on the hanger. After the beam deflected due to the transversal load, the axial load was applied gradually with a linear increase of 89 N, from 0 N to a maximum of 979 N. The value of the applied axial load for Group A, B, and C was checked using simplified beam calculations Eq. (36) as follows and is well below the elastic limit of all specimens:

$$F_{\nu} = \sigma_{\nu} A$$
 (36)

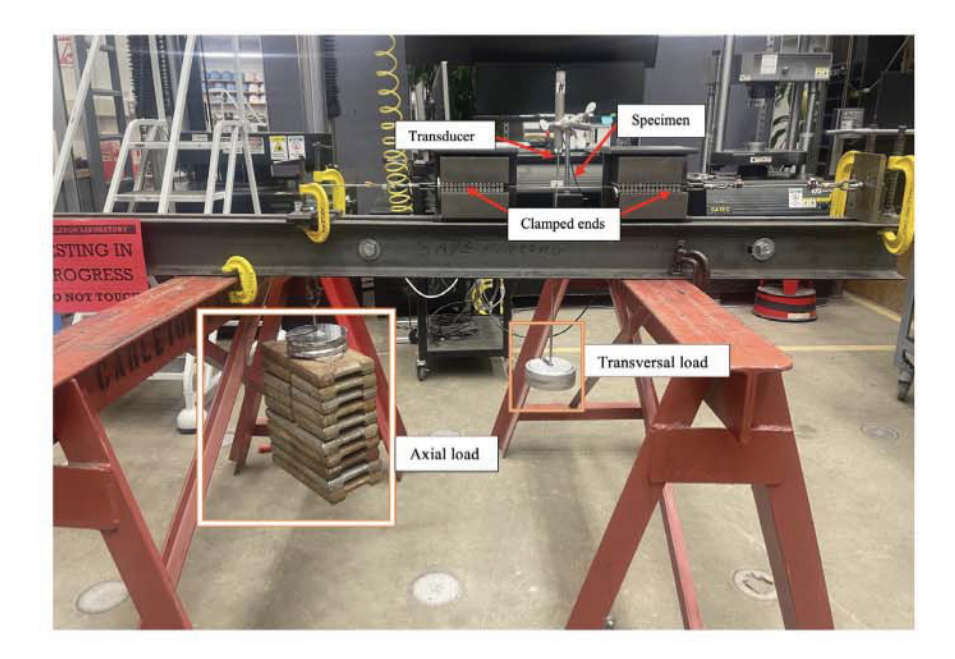


Fig. 7. A clamped beam specimen mounted on a bending and axial stretching test setup.

A maximum of 1/20th, 1/5th and, 1/5th of the tensile capacity was loaded for Groups A, B, and C, respectively. The maximum applied transversal load for Groups A, B, and C was 155.7, 26.7, and 31.1 N, respectively, well below the yielding limit of the elastic beam as well.

4.3. Three-point bending test for the beams with fixed ends

The beam specimens are clamped within two steel blocks with multiple bolts to provide rigid support for rotation and deflection. The blocks are fixed to a steel frame to provide a nearly rigid constraint of horizontal deformation of the aluminum beam specimens. Three-point bending testing was carried out using the Instron Universal Testing Machine on a fully restrained beam to investigate the effect of membrane forces on the deflection of the beam. The experimental setup for the three-point loading is shown in Fig. 8.

Note that although the steel support frame is much stiffer than the thin aluminum beams, the assumption of perfectly rigid support may affect the accuracy due to the small deformation of the steel during the actual experiments.

5. Results and discussion

To validate the formulation, the deflection data obtained from the experiments were compared with the results predicted by the formulation and the results from the numerical simulation using ABAQUS. The beams are modeled as a solid element using quadrilateral CPS4R elements. The beams were modeled to replicate the experimental tests and the material properties listed in Table 1 were used for the FEM models. A concentrated point load is added at the mid-span point and axial tensile load were defined for Group A, B and C. For beams in Group D, fully fixed boundary conditions were defined and the beams were subjected to axial loads at the midpoint. The schematic diagram of finite element model is shown in Fig. 9 and the deflected shape of a fully restrained beam, D1, is shown in Fig. 10

The analytical solutions for the roller-supported and double-clamped beams were computed for a constant transversal load and linearly varying tensile forces. The deflection results were plotted against the applied axial load while keeping the transversal load constant. The



Fig. 8. Three-point bending test setup for the beams with fixed ends.

analytical results are then compared to the values obtained from the experimental results and FEM simulation results .

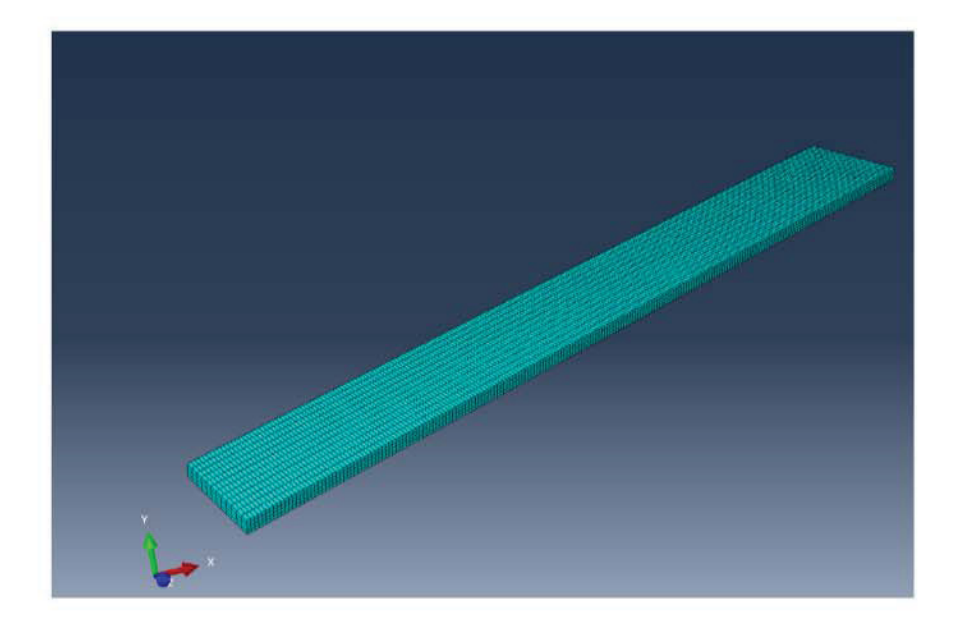


Fig. 9. Schematic diagram of finite element model.

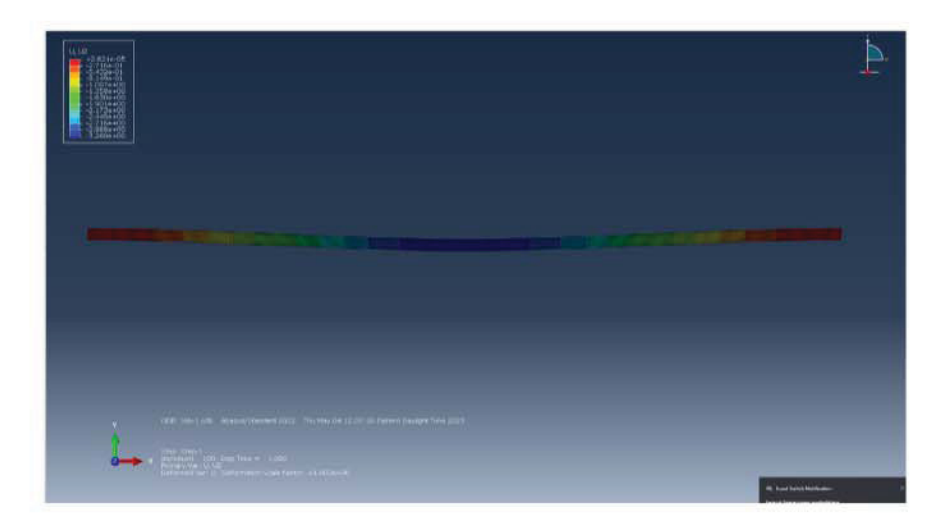


Fig. 10. Displacement contour for restrained beam, D1.

Figs. 11 and 12 show a comparison of the deflections obtained from the analytical solution, FEM and experimental tests for the roller-supported beams for Groups A and B, respectively. The transversal load applied for groups A and B is a constant load of 155.7 and 26.7 N, respectively. Note that the classic beam theory only considers the effect of the transversal load and is not sensitive to the axial load at all. From the figures, it can be seen that there is a good agreement between the three sets of results, with the maximum difference between the deflections being 10% and 15% for Groups A and B, respectively. The errors may be caused by the load transfer efficiency in the testing fixture in Fig. 6 and the plane assumption in the beam's theory. From the graphs, it can be clearly seen that the maximum deflection decreases non-linearly with increasing tensile force. As the axial load P increases from 0 to 980 N, the maximum deflection of the beams reduces by approximately 45% and 87%, for group A and group B, respectively.

For the double-clamped beams, Fig. 13 shows a comparison of the deflections obtained from analytical solution, FEM and experimental

tests. The transversal load applied is constant, 31.1 N. The deflections obtained from the analytical solution and the experiments are very similar. From the graph, when axial load, P increases from 0 to 980 N, the maximum deflection of the beam reduces by approximately 60%.

In addition, the relationship between the maximum deflection and the applied axial tension force P shows that the maximum deflection decreases non-linearly with increasing axial tension force.

For the restrained beams, Beam D1 and D2, the deflection calculated using the classic B–E beam theory, FEM and the new formulation were compared with the experimental results in Figs. 14 and 15, respectively. The relationship between the applied transversal load and the maximum deflection is linear for the classic beam theory, while the experimental results, FEM and the formulation show nonlinear behavior as the load increases. The new formulation captures the nonlinearity of the experimental data very well. The results from the experiment and the classic beam theory are similar for smaller loads, but the structure becomes stiffer as the load increases due to the

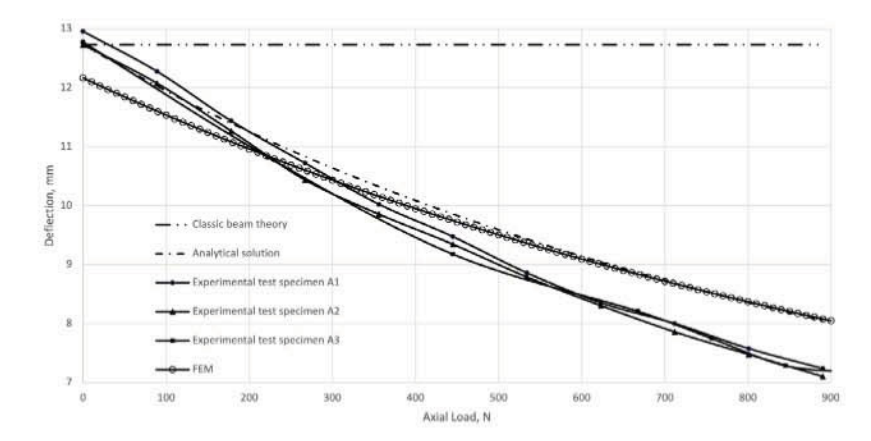


Fig. 11. Relationship between maximum deflection and applied axial tension force P, Group A.

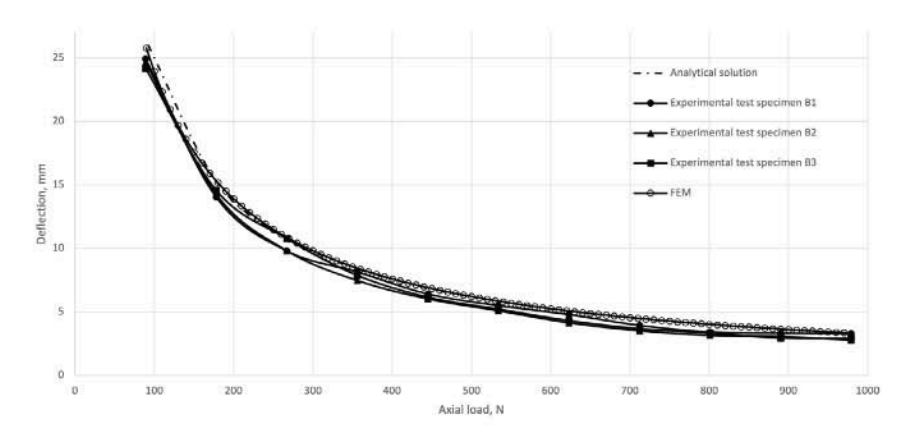


Fig. 12. Relationship between maximum deflection and applied axial tension force P, Group B, a pre-load of 89N is applied to settle the testing sample.

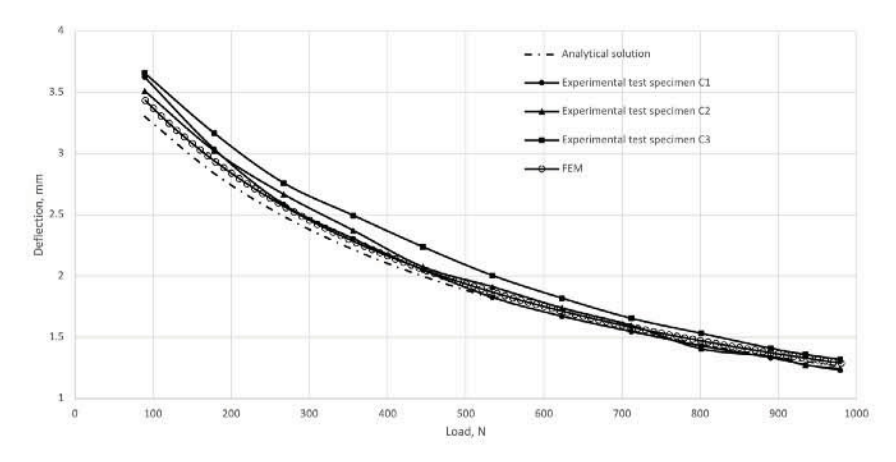


Fig. 13. Relationship between maximum deflection and applied axial tension force P, Group C.

membrane force. The classic beam theory does not consider the effect of the membrane force and thus does not capture the nonlinear behavior well and overestimates the deflection. The deflection calculated by the classic beam theory for 500 N transversal load is 38% higher than that of the experimental deflection, hence proving the significance of considering membrane forces in the deflection calculation of axially restrained beams.

Overall, the present formulation captures the nonlinear elastic behavior of the beams with horizontal constraints or axial tension, which shows the maximum deflection of beams can reduce significantly even when the load is in the elastic range. Another example of the tension member in the structure is a long-span cable, in which the maximum deflection can also be controlled by the axial tension. However, the stress distribution in the cross-section of the cable is assumed to be uniform, so the effect of bending is not considered. The present model fills the gap between the cable and classic beam theories so that both tension and bending effects are well captured. As the axial tension reduces the deflection and stiffens the beam, the combination of the transverse loading and axial tension leads to more complex deformation, and the superposition principle is not applicable even though the beam is still under elastic deformation because the interaction between the two loads produces a nonlinear elastic deformation. This phenomenon can be used to reduce the deflection of large-span structures. Particularly in the lightweight railway structure, the rail sagging under the vehicle loading will be significant for riding comfort and efficiency. The application of the present formulation in the design of

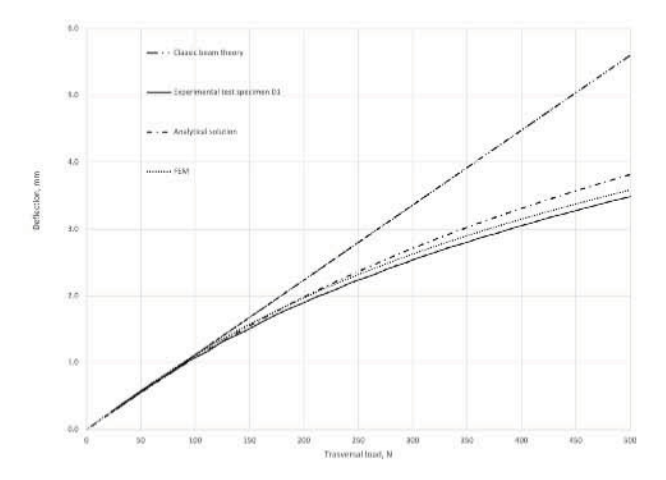


Fig. 14. Relationship between maximum deflection and transversal force for a restrained beam, Specimen D1.

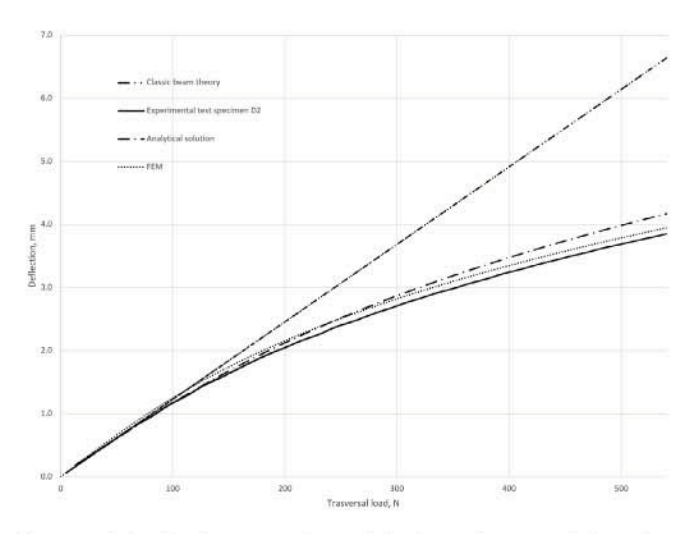


Fig. 15. Relationship between maximum deflection and transversal force for a restrained beam, Specimen D2.

a lightweight rail for the aerial PRT system [2,31] is shown in the next section.

6. Application to aerial PRT design with a smart cushion

6.1. Design of the PRT structure

The structural performance criteria for the design of PRT systems include the stress analysis to avoid strength failure at the extreme loading scenario and the serviceability requirement to satisfy the deflection limit. Due to the relatively long load transferring path of the rail-beam-girder-column-foundation, the sagging of the rail under the pod loading will be particularly important for riding comfort and safety. The rail beams are usually designed for the deflection serviceability requirement using the classic B-E beam theory, but this theory fails to recognize the significant effect of axial restraints on the deflection of beams. Thereby, overestimating the deflection leads to inefficient design and material wastage, which further increases the self-weight of the structure. To improve the design of these rail beams, a new smart mounting system is proposed in this section [2,31]. This smart mounting system is designed to stiffen the rail supporting the autonomous vehicles, which enables large spans between footings and high energy efficiency of the system with improved riding comfort.

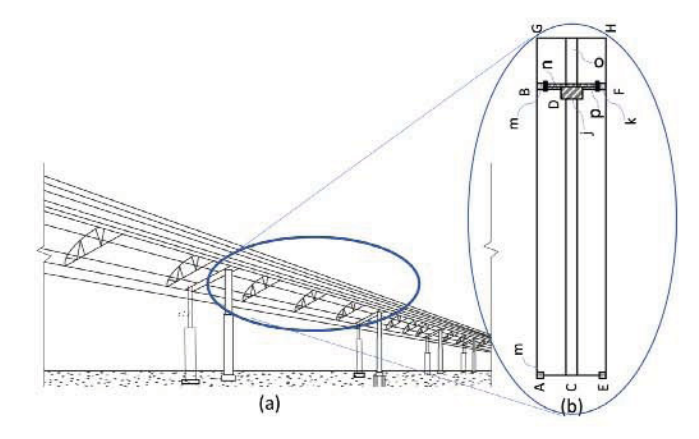


Fig. 16. Schematic structure design of the PRT: (a) Personal rapid transit system; (b) a pre-tensioned PRT rail with a smart cushion.

Fig. 16 shows the schematic structure design of the guideway connecting with the PRT structure through the smart cushion. The pretension frame AB supports a section of the guideway AB between two supporting piles m. Note that the superstructure can be installed by modular construction with pre-fabricated frames including the solar roof and rail beams, so that the PRT system can be rapidly constructed with minimized interruption to surface traffic. The end for each section can be supported by a single pile in Fig. 1 or double piles in Fig. 16. The neighboring sections shall be well-connected so that the vehicle can move through the guideway smoothly with high structural integrity and stability.

The frame AB is connected with neighboring girders AE and p throughout the guideway AB by the force-sensitive connecting bolts. The girders p and AE are connected to a central beam CD to distribute the load on the piles m to the ground. The first girder AE is fixed on the supporting piles m and k, and the other girder p is supported by a roller that allows for horizontal motion. Rigid connections are fabricated between the girders AE, p and frame AB and between the first girder AE and the central beam CD during manufacturing. A smart cushion j, is installed between the second girder p and the central beam CD. The central beam CD uses a smart cushion to provide a compressive force to the central beam CD and to elongate the frame AB. The smart cushion adjusts the length of the guideway section based on changes in environmental temperature.

At an initial condition, the geographic region's highest working temperature T_h is determined. For example, $T_h = 50~^{\circ}\mathrm{C}$ for New York state. The length of the frame AB at $T_h = 50~^{\circ}\mathrm{C}$ is calculated as L_h . Suppose on the date of the installation, the temperature differs. In that case, the smart cushion D is used to adjust the length to L_h , which means when the temperature reaches T_h , the smart cushion D exhibits zero force.

Frame AB can be installed using modular construction. Frame AB with length L_h is installed onto the piles m with sufficient horizontal support to stabilize frame AB. The connecting bolts o are used to link frame AB and frame BG together. The connecting bolts o are pressure sensitive. The installation pressure (or tension force in the bolt) is given at T0. The frames can be installed with substantially zero gaps between frame AB and frame BG so that the pods can drive smoothly on the guideway.

When the temperature changes, the bold pressure T0 shifts to T. This triggers the smart cushion p to adjust the elongation of the frame AB such that the pressure on the connecting bolts O can recover to T0. In this manner, the frame AB functions as a pre-tension mechanism. The pre-tension mechanism is applied to the modular construction of the guideway structure. The pre-tension of the rail is monitored and controlled according to predetermined parameters under different

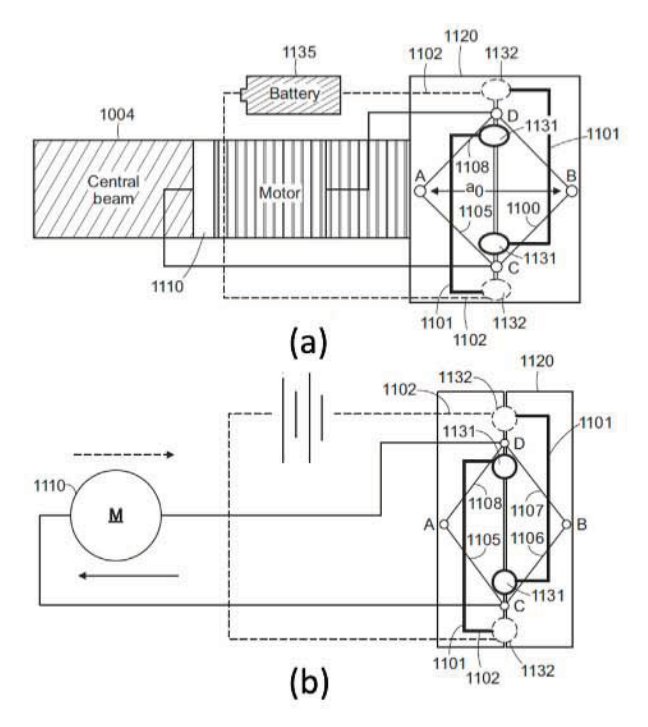


Fig. 17. The smart cushion (a) smart cushion coupled to the central beam (b) the electrical circuit to control the spacing.

seasons or ambient temperature changes such that the rail gap between frame AB and frame BG remains nearly zero.

In summary, the pre-tension in the guideway reduces the sagging at a ratio of 50–90% depending on the length of the frame AB and the weight of the pods that will move through the frame, which will increase the driving energy efficiency and riding comfort as well. Due to the reduced sagging, longer spans of the supporting structure may be used for different road conditions, which significantly reduces the construction difficulty and costs.

6.2. Mechanism of the smart cushion

Fig. 17(a) illustrates the smart cushion J shown on Fig. 16 coupled to the central beam CD; and Fig. 17(b) shows the electrical circuit to control the spacing between the second girder p of frame AB and the first girder n of frame BG by the smart cushion j. Referring to Fig. 17(a), the smart cushion j includes a rhombus-shaped frame 1120 with four hinge points A-D, each of which is free to rotate around a hinge center point. A first horizontal hinge point A is fixed on the second girder p of the frame AB, and a second horizontal hinge point B is fixed on the first girder n of the adjacent frame BG. The two vertical hinge points C-D are able to move toward or away from each other as the gap between the girders p and n increases or decreases, respectively. The horizontal hinge point A and vertical hinge point D are fixed on the girder p and the girder n respectively, with a distance a_0 during the installation of the frame AB and BG. Links 1105-1108 are installed between the hinge points A-D and are configured at an equal angle of 90 degrees. Therefore, the distance between the points C and D is also

The smart cushion *j* includes two pairs of electrodes 1131–1132 coupled to a motor 1110 with a screw block. A first pair of electrodes 1131 is installed on the inside distance between the vertical hinge points C–D. A second pair of electrodes 1132 is installed on the outside distance between the vertical hinge points C–D. The electrodes 1131–1132 are configured along a line consistent with vertical hinge points C–D and exhibit a distance (e.g., approximately 0.2 mm, based on a

sensitivity requirement) between the electrodes 1131–1132 and the closest electrode at point C or D. A battery 1135 is connected to the electrodes 1131–1132. The electrodes 1131–1132 function as a switch for the motor 1110, as described below.

When the frame AB experiences contraction due to a temperature decrease, the distance between the girder p and the girder n increases from their initial distance. As a result, the distance between the horizontal hinge points A-B increases from their initial distance, and the vertical hinge points C-D move toward each other. When the vertical hinge points C-D touch the inside electrodes 1131, the electrodes 1131 complete a first circuit 1101 and triggers the motor 1110. As illustrated in Fig. 17(b), a current flows from the inside electrodes 1131 to the motor 1110, causing the motor 1110 to move the girder P away from the central beam CD, increasing the force on the central beam CD, and increasing the distance between the girder p and the girder AE. This causes the girder P to move closer to the girder n so that the distance between the horizontal hinge points A-B decreases. When the horizontal hinge points A-B recover their initial distance, the vertical hinge points C-D disengage from the electrodes 1131, turning off the motor 1110.

On the other hand, when the frame AB experiences an expansion due to temperature increase, the opposite happens, and the girder p moves away from the girder p so that the distance between the horizontal hinge points A-B increases. When the horizontal hinge points A-B recover their initial distance, the vertical hinge points C-D disengage from the electrodes 1132, turning off the motor 1110.

6.3. Design of a lightweight rail for PRT

In this section, the formulation is applied to design a lightweight rail for the solar personal rapid transit (PRT) system [2,31]. A case study of a restrained lightweight rail with a span of 5 m for a vehicle of 8900 N positioned at the mid-span is designed for an allowable deflection of 50 mm. The beam is made out of Low carbon steel with a yield strength of 345 MPa and 200 GPa elastic modulus. The width of the beam is 100 mm.

As shown in Fig. 18 a and b, the rail deflection was checked for two depths, 34 mm, and 41 mm, respectively. Using the classic beam theory, Eq. (35), for a beam depth of 34 mm, the deflection calculated is 88.51 mm, however when the horizontal constraints are considered, the deflection is 50 mm, which makes a 43% reduction in deflection. Therefore 34 mm depth does satisfy the deflection requirements, but if the classic beam theory is used for design, a depth of 43 mm will be required to fulfill the deflection limit. This leads to a 17% decrease in the depth of the beam. Hence it can be concluded that by including the effect of horizontal constraints, we can design more efficient and economical sections. In addition, it is evident that the impact of horizontal constraints is very significant and should be considered in beam design; this was further validated by including FEM analysis as shown in Fig. 18.

7. Conclusions

The governing equation and the Green's function for the deflection of a roller-supported and double-clamped beam have been derived using the principles of the B–E beam theory for a combined system of transversal and tensile axial loads. The validity of the analytical solution was independently confirmed by cross-checking the results against those obtained from experimental testing and FEM simulations. From the results, it can be concluded that the maximum deflection decreases non-linearly with increasing axial tension force. In addition, an analytical solution using the Green's function for a restrained beam was calculated and compared against experimental results, FEM analysis and the classic beam theory. The experimental results, FEM and the analytical solution, show a nonlinear relationship between the load and the deflection. This nonlinearity is caused by the membrane force,

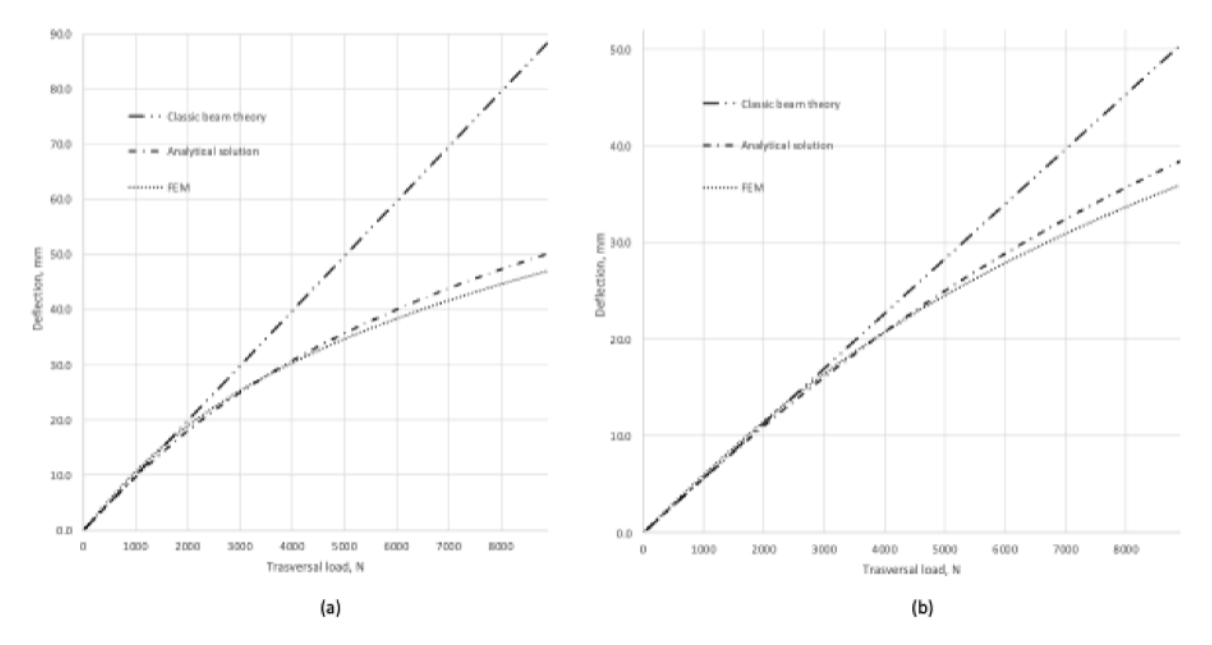


Fig. 18. Relationship between maximum deflection and vehicular point load for a PRT beam with (a) 34 mm depth (b) 41 mm depth.

resulting in the beam's length change due to curling. The classic beam theory fails to consider the membrane forces' effect, hence overestimating the deflection. Therefore, The theoretical model presented in this study could be fundamental to understanding the nonlinear behavior of restrained beams and can provide the basis for the structural design and analysis of restrained beams. In addition, the study showed that beams could be stiffened by providing horizontal restraints, revealing its applicability in aerial PRT by using smart cushions.

CRediT authorship contribution statement

Linda Teka: Writing – original draft, Writing – review & editing, Data curation, Visualization, Investigation. **Liming Li:** Investigation, Validation. **Huiming Yin:** Conceptualization, Methodology, Supervision, Writing – review & editing.

Declaration of competing interest

The authors declare that they have no known competing financial interests or personal relationships that could have appeared to influence the work reported in this paper.

Data availability

Data will be made available on request.

Acknowledgments

This work is sponsored by the National Science Foundation IIP #1738802, IIP #1941244, CMMI #1762891, and U.S. Department of Agriculture NIFA #2021-67021-34201, whose support is gratefully acknowledged. The authors thank Mr. Yanchu Zhang and Mr. Lucas Grafals for sharing some relevant results and Mr. James Basirico for the help with the experiment setup. We are grateful to our industry collaborators at Solar Mobility, including Mr. Frank Pao, Joe Moressey, Jason Lou, and Yuanguo Chen, for sharing the solar PRT system's design, patent, and drawings.

References

- Irving JH, Bernstein H, Olson C, Buyan J. Fundamentals of personal rapid transit. Lexington, MA: Lexington Books; 1978.
- [2] Yin H, Zadshir M, Pao F. Building integrated photovoltaic thermal systems: Fundamentals, designs and applications. Academic Press; 2021.
- [3] Fichter D. Individualized automatic transit and the city. Chicago, IL: B.H. Sikes; 1964.
- [4] ASCE. Automated people mover standards Part 2. ASCE; 2008.
- [5] Liu R. Spectrum of automated guideway transit (AGT) technology and its applications. In: Handbook of transportation engineering. Vol. 2. McGraw-Hill; 2010.
- [6] Anderson JE. How to design a PRT guideway. In: Automated people movers. 2009, p. 436–49.
- [7] Anderson JE. An intelligent transportation network system: Rationale, attributes, status, economics, benefits, and courses of study for engineers and planners. PRT International. LLC: 2009.
- [8] Berger T, Sallez Y, Raileanu S, Tahon C, Trentesaux D, Borangiu T. Personal rapid transit in an open-control framework. Comput Ind Eng 2011;61(2):300–12.
- [9] McDonald SS. Personal rapid transit and its development. In: Transportation technologies for sustainability. Springer; 2013, p. 831–50.
- [10] Anderson JE. Control of personal rapid transit system. Telektronikk 2003;99(1):108–16.
- [11] Anderson JE. Control of personal rapid transit systems. J Adv Transp 1998;32(1):57–74.
- [12] Timoshenko S, Woinowsky-Krieger S. Theory of plates and shells. McGraw-hill New York; 1959.
- [13] Elishakoff I. Who developed the so-calledTimoshenko beam theory? Math Mech Solids 2020;25(1):97–116.
- [14] Labuschagne A, van Rensburg NJ, Van der Merwe A. Comparison of linear beam theories. Math Comput Modelling 2009;49(1–2):20–30.
- [15] Timoshenko S. History of strength of materials: with a brief account of the history of theory of elasticity and theory of structures. Courier Corporation; 1983.
- [16] Bauchau OA, Craig JI. Euler-Bernoulli beam theory. Struct Anal 2009;173–221.
- [17] Wang C, Reddy JN, Lee K. Shear deformable beams and plates: Relationships with classical solutions. Elsevier; 2000.
- [18] Cowper G. The shear coefficient in Timoshenko's beam theory. J Appl Mech 1966;33(2):335–40.
- [19] Timoshenko SP. On the transverse vibrations of bars of uniform cross-section. Lond Edinb Dubl Philos Mag J Sci 1922;43(253):125–31.
- [20] Li Y, Xie L, Zhang T, Wu Y, Sun Y, Ni Z, et al. Mechanical analysis of photovoltaic panels with various boundary condition. Renew Energy 2020;145:242–60.
- [21] Teka LG, Zadshir M, Yin H. Mechanical analysis and design of large building integrated photovoltaic panels for a seamless roof. Sol Energy 2023;251:1–12.
- [22] Manes A, Porcaro R, Ilstad H, Levold E, Langseth M, Børvik T. The behaviour of an offshore steel pipeline material subjected to bending and stretching. Ships Offshore Struct 2012;7(4):371–87.

- [23] Kristoffersen M, Langseth M, Børvik T. Combined three-point bending and axial tension of pressurised and unpressurised X65 offshore steel pipes-Experiments and simulations. Mar Struct 2018;61:560-77.
- [24] Kristoffersen M, Børvik T, Langseth M, Ilstad H, Levold E. Transverse deformation of pressurized pipes with different axial loads. In: International conference on offshore mechanics and arctic engineering. Vol. 57663. ASME; 2017. V03BT02A050
- [25] Zhao O, Rossi B, Gardner L, Young B. Behaviour of structural stainless steel cross-sections under combined loading-Part I: Experimental study. Eng Struct 2015;89:236–46.
- [26] Zhao O, Rossi B, Gardner L, Young B. Behaviour of structural stainless steel cross-sections under combined loading–Part II: Numerical modelling and design approach. Eng Struct 2015;89:247–59.
- [27] Cicirello A, Palmeri A. Static analysis of Euler-Bernoulli beams with multiple unilateral cracks under combined axial and transverse loads. Int J Solids Struct 2014;51(5):1020–9.
- [28] Chen W, Luo L, Guo Z, Yuan P. Experimental studies on load-carrying capacity of HFR-LWC beams accompanying membrane action. Eng Struct 2021;228:111497.
- [29] Chen L, Fang Q, Guo Z, Liu J. An improved analytical method for restrained RC structures subjected to static and dynamic loads. Int J Struct Stab Dyn 2014;14(01):1350052.

- [30] Chen W, Luo L, Guo Z, Wang Y. Load-carrying capacities of fully clamped RC slab accompanying compressive-Tensile membrane actions: A Theoretical Approach. Int J Struct Stab Dyn 2020;20(08):2050094.
- [31] Yin H, Pao F, Lou J, Zadshir M. Solar personal rapid transit system with autonomous pods - Building integrated photovoltaic thermal systems. 2022, U.S. Patent App. 63248502.
- [32] Gustafsson J, Lohmann R, Lowson M. Personal rapid transit: Live applications challenges. Urban Public Transp Syst 2013;347–56.
- [33] IEC63092-1-2020. Photovoltaics in buildings Part 1: Requirements for buildingintegrated photovoltaic modules. International Electrotechnical Commission; 2020.
- [34] IEC63092-2-2020. Photovoltaics in buildings Part 2: Requirements for buildingintegrated photovoltaic systems. International Electrotechnical Commission; 2020.
- [35] Wierzbicki T. Structural mechanics. 2013, https://ocw.mit.edu/courses/2-080jstructural-mechanics-fall-2013/. Chapter 6, Last accessed on 2023-05-17.
- [36] Yin H, Zhao Y. Introduction to the micromechanics of composite materials. CRC Press; 2016.
- [37] Yin H, Song G, Zhang L, Wu C. The inclusion-based boundary element method (iBEM). Academic Press; 2022.
- [38] Young WC, Budynas RG, Sadegh AM. Roark's formulas for stress and strain. McGraw-Hill Education; 2012.